JCEC
THE JOURNAL OF ENGINEERING AND EXACT SCIENCES

OPEN ACCESS

The Journal of Engineering and Exact Sciences – jCEC, Vol. 12 N. 01 (2026)
journal homepage: https://periodicos.ufv.br/jcec
eISSN: 2527-1075
ISSN: 2446-9416

Comparative study of turbulence models in a subsonic educational wind tunnel

Estudo comparativo de modelos de turbulência em túnel de vento didático subsônico

Article Info:
Article history: Received 2026-01-02 / Accepted 2026-03-20 / Available online 2026-03-25
doi: 10.18540/jcecvl12iss1pp23508

Natália de Oliveira Faria
ORCID: https://orcid.org/0000-0003-3735-1085
Universidade Federal de Viçosa, Brazil
E-mail: natalia.o.faria@ufv.br
Julio Cesar Costa Campos
ORCID: https://orcid.org/0000-0002-9488-8164
Universidade Federal de Viçosa, Brazil
E-mail: julio.campos@ufv.br
Charles Luís da Silva
ORCID: https://orcid.org/0000-0003-1558-0485
Universidade Federal de Viçosa, Brazil
E-mail: charles.silva@ufv.br
Rogério Fernandes Brito
ORCID: https://orcid.org/0000-0002-6833-7801
Universidade Federal de Itajubá, Brazil
E-mail: rogbrito@unifei.edu.br
Antonio Marcos de Oliveira Siqueira
ORCID: https://orcid.org/0000-0001-9334-0394
Universidade Federal de Viçosa, Brazil
E-mail: antonio.siqueira@ufv.br
Henrique Márcio Pereira Rosa
ORCID: https://orcid.org/0000-0002-1437-2265
Universidade Federal de Viçosa, Brazil
E-mail: henrique.rosa@ufv.br
Álvaro Messias Bigonha Tibiriçá
ORCID: https://orcid.org/0000-0002-3300-1988
Universidade Federal de Viçosa, Brazil
E-mail: alvaro.tibirica@ufv.br
Washington Orlando Irrazabal Bohorquez
ORCID: https://orcid.org/0000-0002-9762-0665
Universidade Federal de Juiz de Fora, Brazil
E-mail: washington.irrazabal@ufjf.edu.br

Abstract
This study presents the design of an open-circuit, suction-type subsonic wind tunnel and a comparative evaluation of three turbulence models: Shear Stress Transport (SST) k-omega, Realizable k-epsilon, and Spalart-Allmaras. The main components of the wind tunnel, including the test section, diffuser, and contraction nozzle, were designed using a combined cubic profile for the contraction geometry. Empirical correlations were applied to estimate pressure losses throughout the system. The internal flow behavior was analyzed using computational fluid dynamics (CFD) simulations with the three turbulence models. The final design resulted in a wind tunnel with a total

length of 6.36 m, a square test section with a side length of 0.56 m, and a design velocity of 63 m/s. Numerical results showed good agreement with analytical predictions, with deviations below 0.4% for the test section velocity and below 1.3% for the dynamic pressure at the test section inlet. Velocity contours, dynamic pressure distributions, and velocity profiles showed strong agreement among the turbulence models, indicating low sensitivity of the flow to the turbulence model under the studied conditions. Among the evaluated models, the Spalart-Allmaras model provided accuracy comparable to the others while requiring lower computational cost, making it the most suitable model for this type of analysis.
Keywords: Wind tunnel; Computational fluid dynamics; Spalart-Allmaras; Realizable k-epsilon; SST k-omega.

1. Introduction

Aerodynamics is a fundamental field of fluid mechanics responsible for investigating the interactions and forces that gases, especially air, exert on objects. This area of study gained prominence in the 20th century, particularly during the interwar period, when the need to enhance performance and reduce fuel consumption in cars and aircraft increased (Matos, 2008). However, the application of aerodynamic principles extends far beyond terrestrial and aerial vehicles (Barbosa *et al*., 2021).

Currently, research in aerodynamics is primarily driven by the quest for greater performance, agility, operational cost reduction, and noise mitigation. Consequently, the study of airflow and its implications have become essential in various fields, ranging from the aerospace and automotive industries to construction and the development of special devices such as parachutes and sports equipment. For example, Souza *et al*. (2023) experimentally analyzed the aerodynamic behavior of tennis balls in wind tunnels, demonstrating how different geometric parameters can directly impact sports performance.

To understand these phenomena and predict the forces involved in interactions between fluids and solid bodies, various investigative methods are employed. These methods combine experimentation, theory, and computational simulations, which gained momentum starting in the 1960s. While it was expected that the integration of theoretical and computational methods would provide detailed design guidance in many practical problems, simulations still represent simplifications of the reality of the phenomenon. Thus, despite significant advancements in computational capability, experimental tests remain the primary source for final and refined decisions by designers in many applications. In this context, the wind tunnel stands out as the main equipment of experimental aerodynamics for model validation (Barlow *et al*., 1999). As highlighted by Reddy and Subramanian (2025), a conventional subsonic wind tunnel is an essential tool for both fundamental research in fluid dynamics and for validating mathematical models and numerical codes, in addition to enabling tests of models or prototypes intended for the development of engineering devices that interact with airflow. Given this relevance, understanding the structure and operation of wind tunnels becomes fundamental.

Wind tunnels primarily function to simulate the behavior of air in relation to solid objects. They come in different shapes and sizes and can generally be classified according to their geometry, speed range, and flow direction. Although experimental tests are indispensable for model validation, integrating this method with numerical simulations represents the most suitable approach as it allows for obtaining more precise and reliable results.

In this context, the comparison between different turbulence models becomes particularly relevant. The Spalart-Allmaras, Realizable k-ε, and Shear-Stress Transport (SST) k-ω models were selected for having distinct characteristics that make them suitable for different flow conditions, in addition to representing three of the most commonly used formulations in industrial applications and research in aerodynamics. Thus, these models encompass different levels of complexity, computational cost, and capacity to predict essential flow characteristics, allowing for a comprehensive and well-founded comparative analysis.

Therefore, considering the relevance of experimental and computational methods for analyzing problems, the present article aims to size a subsonic educational wind tunnel and perform computational fluid dynamics simulations using three distinct turbulence models: Spalart-Allmaras, Realizable k-ε, and SST k-ω.

2. Theoretical Background

Studies such as those conducted by Barlow *et al*. (1999), Bell and Mehta (1989), Lins (2018), and Zart *et al*. (2018) address the design and analysis of wind tunnel components, which are essential for proper operation and for ensuring the reliability of experimental results.

In the present study, particular emphasis is placed on the test section, the contraction nozzle, and the diffuser, followed by the evaluation of the corresponding total pressure losses. Additionally, the turbulence models Spalart-Allmaras, Realizable k-ε, and SST k-ω, which are employed in the computational simulations, are discussed.

2.1 Pressure Loss

Each wind tunnel component, except for the fan and propeller, is subject to pressure losses, since mechanical energy is partially converted into thermal energy due to viscous effects between the airflow inside the tunnel and the solid surfaces in contact with it.

The pressure loss across a wind tunnel component is defined as the mean reduction in total pressure of the flow after passing through a given section (Barlow *et al*., 1999).

According to Pereira (2011), the total pressure loss of the wind tunnel (Δp_{total}) can be determined as the sum of the pressure losses of each individual component and expressed as the product of a loss coefficient and the dynamic pressure at the component inlet, as shown in Equation 1:

$$\Delta p_{total} = \sum_{i=1}^{n} 0{,}5 \rho V_i^2 k_i \quad (1)$$

where i denotes each wind tunnel component, k represents the local pressure loss coefficient, ρ is the air density, and V is the average velocity at the inlet section of component i.

2.2 Wind Tunnel Design

Wind tunnel design begins with the definition of a reference model that establishes the minimum test section dimensions. This study adopts the standard wing of the AeroDesign team Skywards UFVoa (Federal University of Viçosa) as the reference geometry. The wing has a mean aerodynamic chord $c = 0.45$ mand a semi-span $b = 1.30$ m. The aircraft maximum operating velocity, $V = 21$ m/s, defines the target test section velocity. A geometric scale of $e = 1:3$limits the overall tunnel dimensions while preserving aerodynamic similarity. Although immediate construction is not planned, maintaining realistic geometric parameters ensures future technical feasibility.

The test section is dimensioned after selecting the reference model. Its geometric configuration must ensure adequate accessibility, facilitate model installation, and accommodate instrumentation for data acquisition (Lins, 2018).

To ensure compatibility between the aerodynamic coefficients of the model and the prototype, dynamic similarity of the flow is required. According to Barlow *et al*. (1999), for low-speed wind tunnels, the similarity parameter depends solely on the Reynolds number, which can be calculated as shown in Equation (2).

$$Re = \frac{\rho \cdot V \cdot c}{\mu} \quad (2)$$

where ρ is the air density, V is the velocity, c is the mean chord, and μ is the dynamic viscosity of air é a

Since the Reynolds number must be identical for both the model and the prototype, the required test section velocity (V_{ST}) can be determined from Equation 3.

$$V_{ST} = \frac{Re \cdot \mu}{c \cdot e \cdot \rho} \tag{3}$$

where μ is the dynamic viscosity of air, c is the mean chord, e is the working scale, and ρ is the air density.

The minimum dimension of the test section edge is determined by considering the interference effects between the boundary layers of this component and the model to be tested. Since the wall boundary layer thickness may reach approximately 10% of the test section edge length, a minimum clearance margin of 20% is required (Barlow *et al*., 1999). This condition leads to Equation 4:

$$W_{ST} = \frac{b \cdot e}{0{,}8} \tag{4}$$

where W_{ST} is the minimum dimension of the test section edge, b is the wing semi-span, and e is the working scale.

The pressure loss coefficient of the test section is obtained using Equation 5, as proposed by Fox *et al*. (2010):

$$K_{ST} = f \cdot \frac{L_{ST}}{Dh_{ST}} \tag{5}$$

where L_{ST} is the test section length, $D_{h,ST}$ is the hydraulic diameter, and f is the Darcy friction factor.

The friction factor is determined from the implicit Prandtl–von Kármán relation given in Equation 6.

$$f = [2 \cdot log_{10} \cdot (Re\sqrt{f}) - 0{,}8]^{-2} \tag{6}$$

in which the Reynolds number is evaluated using the hydraulic inlet diameter.

The contraction nozzle defines the quality of the flow entering the test section. It reduces turbulence intensity and enhances flow uniformity (Almeida *et al*., 2018; Su, 1991). Derbunovich *et al*. (1987) showed that the contraction aligns and accelerates the flow. Hussain and Ramjee (1976) demonstrated that it suppresses mean velocity non-uniformities more effectively than longitudinal turbulence, although it may amplify transverse fluctuations. The acceleration produced by the contraction also reduces the required operating power (Kareem *et al*., 2021).

To produce a uniform and stable flow at the exit of a subsonic contraction nozzle, specific geometric design requirements must be satisfied. The contraction nozzle wall profile, typically described by a polynomial function, must present zero first- and second-order derivatives at both ends to ensure smooth flow acceleration and eliminate curvature discontinuities (Mehta & Bradshaw, 1979).

The boundary layer developing along the contraction wall should remain as thin as possible. Shorter contractions limit boundary layer growth and therefore reduce viscous effects. However, excessive reduction of the contraction length increases the risk of boundary layer separation, which may generate flow non-uniformities and instability at the contraction exit (Mathew *et al*., 2005; Mehta & Bradshaw, 1979).

The contraction ratio (R_C), defined as the ratio between inlet and outlet areas, strongly influences flow uniformity and separation risk. For low-speed wind tunnels with test section areas smaller than 0.5 m², recommended values range from 6 to 10 (Barlow *et al*., 1999; Bell & Mehta, 1988).

The ratio between the contraction length (L_{BC}) and the inlet edge dimension (W_{BC}), defined as the contraction aspect ratio (AR_{BC}), should range from 0.89 to 1.79 to prevent boundary layer separation (Bell & Mehta, 1989).

In addition to this constraint, the contraction length must satisfy the geometric criterion expressed in Equation 7, as recommended by Morel (1977).

$$0{,}75 \cdot D_i \leq L_{BC} \leq 1{,}25 \cdot D_i \tag{7}$$

where D_i represents the diameter of the contraction nozzle inlet base. In the case of a square contraction nozzle section, D_i represents the edge length.

The inlet edge dimension of the contraction nozzle is calculated using Equation 8:

$$W_{BC,IN} = W_{ST}\sqrt{R_C} \tag{8}$$

where $W_{BC,IN}$ represents the edge length of the contraction nozzle inlet cross section and R_C is the contraction ratio.

The contraction length can also be expressed in terms of the aspect ratio AR_{BC}, as shown in Equation 9:

$$L_{BC} = W_{ST} \cdot AR_{BC} \tag{9}$$

where L_{BC} is the length, and AR_{BC} is the aspect ratio of the contraction nozzle.

Lins (2018) noted that no universally satisfactory method exists for designing contraction nozzle profiles, and many early designs relied primarily on visual judgment. Bell and Mehta (1988) later formalized these geometries by representing the profiles using third-, fifth-, and seventh-degree polynomial functions.

For axisymmetric contraction nozzles, Assato *et al*. (2004) and Girardi *et al*. (2002) proposed an effective design approach in which the wall profile is divided into two distinct regions described by cubic polynomials, $f_1(x)$and $f_2(x)$, connected at an inflection point (x_m, y_m). In addition to enforcing zero first- and second-order derivatives at the extremities to ensure smooth flow acceleration, the method requires continuity at the inflection point by imposing the condition $f_1(x_m) = f_2(x_m)$.

The contraction pressure loss coefficient follows the relation proposed by Wattendorf (1938), given in Equation 10:

$$K_{BC} = 0{,}32 \cdot f_m \cdot \frac{L_{BC}}{Dh_{S,BC}} \tag{10}$$

where f_m is the mean friction factor based on the average Reynolds number between inlet and outlet sections, and $Dh_{S,BC}$ is the hydraulic diameter at the contraction outlet.

The diffuser, located downstream of the test section, decelerates the flow to recover static pressure and reduce overall energy losses (Arifuzzaman & Mashud, 2012; Oliveira *et al*., 2015; Zart *et al*., 2018).

To minimize boundary layer separation, Barlow *et al*. (1999) recommend a maximum diffuser half-angle of $\alpha_D = 3°$ and a maximum aspect ratio $AR_D = 2.5$. Based on these constraints, the minimum diffuser length (L_D) is determined using Equation 11.

$$L_D = \frac{\sqrt{\frac{4 \cdot AR_D \cdot A_{ST}}{\pi}} - W_{ST}}{2 \cdot \tan(\alpha_D)} \tag{11}$$

where A_{ST} is the cross-sectional area of the test section.

The diffuser diameter (D_D) is calculated according to Equation (12).

$$D_D = 2 \cdot L_D \cdot \tan(\alpha_D) + W_{ST} \tag{12}$$

The total diffuser loss coefficient (K_{DF}) is defined as the sum of the friction loss coefficient (K_f) and expansion loss coefficient (K_{exp}), as expressed in Equation 13 (Barlow *et al*., 1999):

$$K_{DF} = K_f + K_{exp} \tag{13}$$

The friction loss component is calculated using Equation 14 (Barlow *et al*., 1999):

$$K_f = \left(1 - \frac{1}{AR_{DF}^2}\right) \frac{f}{8 \cdot \text{sen}(\theta)} \tag{14}$$

The expansion loss component is obtained from the empirical correlation presented in Equation 15 and depends on the factor $K_e(\theta)$, which is a function of the equivalent conical angle, and on AR_{DF}, which is the ratio between the outlet and inlet areas (Barlow *et al*., 1999).

$$K_{exp} = K_e(\theta) \left(\frac{AR_{DF} - 1}{AR_{DF}}\right)^2 \tag{15}$$

The factor $K_e(\theta)$ depends on the shape of the diffuser cross section and is based on empirical relationships, as given by Equation (16) (Van Dommelen, 2013).

$$K_e(\theta)_{(quadrado)} = \begin{cases} 0{,}09623 - 0{,}004152\theta \text{ para } 0° \leq \theta \leq 1{,}5° \\ 0{,}122156 - 0{,}0458960\theta + 0{,}02202816\theta^2 \\ -0{,}00326915\theta^3 - 0{,}0006144896\theta^4 \\ +0{,}000279990008\theta^5 - 0{,}0000233738888\theta^6 \\ \text{para } 1{,}5° \leq \theta \leq 5° \\ -0{,}1322 + 0{,}05866\theta \text{ para } 5° < \theta \end{cases} \tag{16}$$

2.3 Turbulence Models

Turbulence is an inherently chaotic phenomenon characterized by velocity fluctuations and strong nonlinear interactions across multiple length and time scales. It is present in a wide range of practical engineering flows, including open-cavity flows, bubble dynamics, wind turbines, aircraft aerodynamics, and combustion systems (Treto *et al*., 2020).

No turbulence model is universally superior for all flow configurations (Ansys Inc., 2013). Nonetheless, the appropriate selection of a turbulence model is crucial to ensure that CFD predictions adequately represent the underlying physical behavior of the flow (Çengel & Cimbala, 2007). The choice of model depends on several factors, including the governing flow physics, the required level of predictive accuracy, available computational resources, and time constraints associated with the simulation.

Turbulence modeling approaches are conventionally grouped into three principal categories: Reynolds-Averaged Navier-Stokes (RANS), Large Eddy Simulation (LES), and Direct Numerical Simulation (DNS) (Versteeg & Malalasekera, 2007). The present study employs the RANS approach due to its computational efficiency and its demonstrated suitability for industrial and engineering flow analyses.

RANS Models: The RANS formulation remains the most widely employed turbulence modeling approach in industrial and engineering applications. For most design-oriented analyses, time-averaged flow quantities, such as mean velocity and static pressure, are sufficient to characterize aerodynamic performance (Versteeg & Malalasekera, 2007). Moreover, RANS models

provide a favorable compromise between computational cost and predictive capability (Ansys Inc., 2013).

The RANS formulation represents one of the most widely adopted classes of turbulence models in industrial applications for turbulent flow calculations. For engineering applications, time-averaged flow quantities, such as mean velocity and static pressure, are generally sufficient to characterize flow behavior (Versteeg & Malalasekera, 2007). RANS formulation provides the most computationally economical approach for turbulent flow prediction while delivering the level of accuracy required for a broad spectrum of engineering analyses (Ansys Inc., 2013).

According to Menter *et al*. (2011), Osborne Reynolds proposed an averaging concept for the Navier-Stokes equations that substantially reduces the complexity of turbulent flow simulations. The resulting RANS equations are formulated in terms of the mean flow field, while turbulent fluctuations are removed from the governing equations through the averaging process.

However, as reported by Menter *et al*. (2011), Moreira *et al*. (2014), and Wilcox (1998), the averaging procedure introduces the Reynolds stress tensor into the RANS momentum equations. The presence of this additional term results in a system with more unknowns than governing equations, thereby leading to the classical closure problem of turbulence. The primary objective of RANS turbulence models is to achieve closure by establishing mathematical relationships between the Reynolds stresses and the mean velocity field (Menter *et al*., 2011).

RANS turbulence models are commonly classified according to the number of additional transport equations solved in conjunction with the RANS flow equations (Versteeg & Malalasekera, 2007), as summarized in Table 1.

Table 1 – Classification of RANS turbulence models.

Number of Extra Transport Equations	Model Name
Zero	Mixing Length Model
One	Spalart-Allmaras Model
Two	k-ε Model
Two	k-ω Model
Two	Algebraic Stress Model
Seven	Reynolds Stress Model

Source: Versteeg & Malalasekera (2007).

One-equation turbulence models solve a single partial differential equation that describes the transport of a turbulent scale, typically used to estimate the turbulent viscosity (Rezende, 2009). In this class of models, the turbulent length scale is not computed explicitly; instead, it must be prescribed in order to determine the dissipation rate of the transported turbulent kinetic energy (Versteeg and Malalasekera, 2007).

Two-equation turbulence models, in contrast, allow both the turbulent length and time scales to be obtained through the solution of two separate transport equations (Ansys Inc., 2021). These models are the most widely employed in industrial applications and constitute the principal families adopted in industrial flow simulations (Ansys Inc., 2013; Menter *et al*., 2011). The turbulence models selected for the present study are the Realizable k-ε and the SST k-ω.

The RANS approach is derived from the application of Reynolds decomposition to the Navier-Stokes equations for incompressible flow, yielding governing equations for mean flow quantities (Rezende, 2009). Under this decomposition, instantaneous flow variables are represented as the sum of a mean component and a random fluctuating component about that mean.

Within this statistical framework, the instantaneous velocity component u_j is expressed as the sum of its mean value $\bar{u}_j$ and its fluctuating component u'_j, as shown in Equation 17.

$$u_j = \bar{u}_j + u'_j \tag{17}$$

Accordingly, the Reynolds decomposition may be extended to any flow variable, as presented in Equation 18.

$$\emptyset_j = \overline{\emptyset}_j + \emptyset'_j \tag{18}$$

where $\overline{\emptyset}_j$ represents the mean value and $\emptyset'_j$ characterizes the instantaneous fluctuation about the mean.

Substituting this decomposition into the continuity and linear momentum equations for incompressible flow leads to the RANS equations.

$$\frac{\partial \bar{u}_j}{\partial x_j} = 0 \tag{19}$$

$$\rho \frac{\partial \bar{u}_i}{\partial t} + \frac{\partial \bar{u}_i}{\partial x_j} \rho\left(\overline{u_\iota u_j}\right) = -\frac{\partial \bar{p}}{\partial x_i} + \frac{\partial}{\partial x_j}\left(\mu \frac{\partial \bar{u}_i}{\partial x_j} - \rho \overline{u'_\iota u'_j}\right) + \rho g_i \tag{20}$$

where ρ is the fluid density, $\bar{p}$ is the mean pressure, t is time, μ is the dynamic viscosity of the fluid, g_i is the component of gravitational acceleration in the i, x_j is the spatial coordinate in the j direction, $\bar{u}_i$ and $\bar{u}_j$ represent the mean velocity components in the i and j directions, respectively, while u'_i and u'_j are the fluctuating velocity components in the i and j, directions, respectively.

Equation 20 is commonly referred to as the RANS equation, and the additional term that arises, $-\rho \overline{u'_\iota u'_j}$, is known as the Reynolds stress tensor. This tensor represents the effect of turbulent fluctuations on the mean flow field. As noted by Wilcox (1998), the Reynolds stress tensor is symmetric and therefore contains six independent components that are introduced into the system without the addition of corresponding governing equations. Consequently, the system becomes underdetermined, giving rise to the turbulence closure problem. To overcome this limitation, the introduction of a turbulence model is required.

The Spalart-Allmaras model, originally developed by Spalart and Allmaras (1992), is a one-equation turbulence model that solves a single transport equation for the turbulent viscosity. As a result, the computational effort associated with this formulation is comparatively lower. As discussed by Versteeg and Malalasekera (2007), in one-equation turbulence models the turbulent length scale is not directly computed and must instead be specified in order to determine the dissipation rate of the transported turbulent kinetic energy.

The Spalart-Allmaras model was originally developed for external aerodynamic applications involving wall-bounded flows over solid surfaces. Owing to its formulation, the model typically exhibits improved predictive capability relative to k-ε models in flows subjected to adverse pressure gradients and incipient separation. As noted by Versteeg and Malalasekera (2007), the Spalart-Allmaras model has also been increasingly employed in turbomachinery analyses. Nevertheless, its applicability to more general internal flows is limited, primarily because the appropriate turbulent length scale is not explicitly determined within the model formulation. Santos (2012) further indicates that the model may yield relatively large errors in certain free-shear flows, particularly in circular and planar jets, which restricts its suitability for general industrial flow simulations.

The Ansys Inc. (2013) manual emphasizes that the Spalart-Allmaras model, in its full implementation, is particularly effective for low-Reynolds-number applications. Consequently, the computational mesh within the boundary layer region must be sufficiently refined to ensure an adequate resolution of near-wall flow behavior. The document further states that this refinement should be guided by the dimensionless parameter y^+, which represents the non-dimensional distance from the wall to the first mesh node. For improved numerical accuracy when employing the Spalart-Allmaras model, recommended values are $y^+ \approx 1$ or $y^+ \geq 30$, whereas values in the range $3 < y^+ < 30$ are generally discouraged.

The Realizable k-ε model represents an improved variant of the Standard k-ε turbulence model and employs two transport equations: one for the turbulent kinetic energy (k)and another for the turbulence dissipation rate (ε).

As described by Soares (2013) and Ansys Inc. (2021), the term "realizable" refers to the capability of the model to satisfy certain mathematical constraints on the Reynolds stresses that are consistent with the physics of turbulent flows, which are not satisfied by the Standard and RNG (Renormalization Group) models.

The Realizable k-ε model, proposed by Shih *et al*. (1994), was developed to address deficiencies of the original formulation through two principal modifications. The first consists of adopting a new formulation for the turbulent viscosity that incorporates the variable C_μ, originally introduced by Reynolds. The second involves a modified transport equation for the dissipation rate (ε), derived from the dynamic equation of the mean-square vorticity fluctuation (Ansys Inc., 2021; Soares, 2013). Nevertheless, the Ansys Inc. (2013) manual notes that one limitation of this model is associated with the prediction of nonphysical turbulent viscosities in situations where the computational domain contains both rotating and stationary fluid regions. This behavior arises because the model incorporates the effects of mean rotation in the formulation of the turbulent viscosity. As reported by Dantas (2017), the rotational effects captured by this model are more accurately represented than those predicted by the Standard k-ε model. With regard to near-wall resolution requirements, recommended y^+ values lie within the range $30 \leq y^+ \leq 300$, allowing the turbulence model to properly account for boundary layer effects.

The SST k-ω model was developed by Menter (1994) and also employs two transport equations: one for the turbulent kinetic energy and another for the turbulence dissipation rate or specific dissipation frequency. Versteeg and Malalasekera (2007) and Fiuza and Rezende (2019) explain that this model combines the robustness and near-wall accuracy of the Wilcox k-ω formulation with the far-field performance of the Standard k-ε model. Consequently, as reported by Shelil (2021), the SST k-ω model generally exhibits superior predictive capability compared with the Standard k-ω and Standard k-ε turbulence models.

All variants of the k-ω model share a similar theoretical foundation. However, as described in the Ansys Inc. (2013) manual, the SST k-ω formulation differs from the Standard k-ω model primarily in two aspects:

- Gradual transition from the Standard k-ω model in the inner region of the boundary layer to a high–Reynolds-number k-ε model in the outer region of the boundary layer.
- A modified turbulent viscosity formulation that accounts for the transport of turbulent shear stresses.

These improvements resulted in the SST k-ω model, which provides enhanced accuracy and robustness for a wide range of flow conditions. Typical applications include flows with strong adverse pressure gradients, airfoil aerodynamics, and transonic shock-wave interactions (Dantas, 2017). For the SST k-ω model, a near-wall resolution corresponding to $y^+ \approx 1$ is recommended.

3. Methodology

The methodology employed in this study began with the development of a computational design routine for sizing the main components of the wind tunnel using Matlab© and EES© (Engineering Equation Solver).

The dimensions of the test section were determined from the geometry of the reference model, the selected geometric scale, and the Reynolds number associated with the full-scale configuration. This Reynolds number was used exclusively to determine the required test section velocity, thereby ensuring dynamic similarity between the model and the prototype.

The mathematical description of the contraction nozzle was established by imposing geometric constraints that ensure flow smoothness and continuity. The contraction profile was defined by two curves represented by cubic polynomial functions, connected at an inflection point located at half of the contraction length.

For the diffuser design, empirical relationships were employed to gradually reduce the flow velocity while preventing adverse pressure gradients that could degrade the flow quality in the test section.

After completing the geometric design, pressure losses across the wind tunnel components were estimated using empirical correlations implemented in EES© and in a spreadsheet environment. Three-dimensional models of the wind tunnel components were then created using SolidWorks©.

Following the geometric design stage, pressure losses across the wind tunnel components were estimated using empirical correlations implemented in EES© and spreadsheet calculations. Three-dimensional models of the wind tunnel components were subsequently developed in SolidWorks©.

CFD simulations were then conducted to analyze the internal flow field of the wind tunnel using three turbulence models: Spalart-Allmaras, Realizable k-ε, and SST k-ω. The simulations were performed in ANSYS Fluent© in order to assess the influence of the turbulence model on the velocity and pressure fields as well as on the overall pressure losses.

For spatial discretization, a MultiZone meshing strategy was employed. This approach enables the automatic decomposition of the computational domain into structured and unstructured regions, which is particularly advantageous for geometries where the generation of a fully structured mesh is impractical. In near-wall regions, prismatic layers generated through the Inflation tool were applied to adequately resolve the boundary layer and improve the accuracy of the numerical solution.

Mesh quality was assessed using the skewness metric, which is highly sensitive to element distortion and directly associated with numerical stability. This parameter quantifies the deviation of a cell from its ideal geometric configuration. A value of 1 corresponds to a fully distorted element, whereas a value of 0 represents an ideal equilateral element (Ansys Inc., 2021). In the present study, a maximum skewness value of 0.60 was considered acceptable.

Several simplifying assumptions were introduced in the CFD analysis. Although real fluids exhibit density variations, these variations remain below approximately 5% for Mach numbers lower than 0.3. Under such conditions, density variations may be neglected without significantly affecting the flow solution. Since the wind tunnel designed in this work operates under subsonic conditions and is intended for didactic purposes, the incompressible flow assumption was adopted. Furthermore, although fluid flows are inherently unsteady, a steady-state formulation was considered adequate because the objectives of the present analysis are not strongly influenced by transient effects.

Regarding the boundary conditions, the contraction inlet surface was defined as a mass-flow inlet with a prescribed mass flow rate of 24.20 kg/s. The diffuser outlet surface was specified as a pressure outlet with the static pressure set to ambient conditions. All wind tunnel surfaces were modeled as no-slip walls. A turbulence intensity of 5% was imposed at the inlet boundary in order to represent the turbulence-generating effects of screens and honeycombs, which were not explicitly modeled in the computational domain.

For the numerical solution procedure, the SIMPLEC (Semi-Implicit Method for Pressure-Linked Equations-Consistent) algorithm was employed for pressure-velocity coupling. Air was defined as the working fluid with the standard properties available in ANSYS Fluent© ($\rho = 1.225$ kg/m³ and $\mu = 1.7894 \times 10^{-5}$ kg/(m·s)).

For spatial discretization, the Least-Squares Cell-Based scheme was employed for gradient evaluation. The Second-Order Upwind scheme was used for the discretization of the transport equations, while pressure interpolation was performed using the Standard scheme. Although the PRESTO (Pressure Staggering Option) scheme is generally recommended for domains with pronounced curvature, it was not adopted in the present simulations due to its higher computational cost.

The High Order Term Relaxation option was enabled to enhance numerical stability. Convergence was assumed when the residuals of the governing equations decreased to the order of

10^{-5}. In addition, monitoring points were defined for static and total pressure at the wind tunnel inlet, as well as for velocity at the entrance of the test section, in order to ensure solution convergence. A maximum of 4000 iterations was prescribed for each turbulence model considered: Spalart-Allmaras, Realizable k-ε, and SST k-ω.

4. Results and Discussion

The analysis was conducted based on the component sizing procedure, the three-dimensional modeling, the evaluation of pressure losses, and the computational simulation of the wind tunnel.

4.1 Component Dimensioning

Test section: A square test section was selected due to its geometric simplicity, which facilitates the development of the three-dimensional model and enables the generation of structured meshes with improved uniformity and quality control. The Reynolds number was calculated using Equation 2, resulting in $Re \approx 6.47 \times 10^5$. This value was used exclusively to determine the required velocity in the test section, which was calculated using Equation 3 as $V_{ST} = 63$ m/s, considering the working scale of $e = 1:3$ and the maximum velocity of the full-scale model, equal to 21 m/s. Equation 4 was used to determine the dimension of the test section edge, resulting in $W_{ST} = 0.542$ m. However, since Equation 4 provides a minimum value, a rounded dimension of $W_{ST} = 0.56$ m was adopted. In addition, the length of the test section was defined as $L_{ST} = 1.1$ m.

Diffuser: The diffuser aspect ratio and half-angle were defined following the recommendations of Barlow *et al*. (1999), and the values $AR_D = 2.1$ and $\alpha_D = 2.75°$ were adopted. Substitution of these parameters into Equations 9 and 10 yielded a diffuser length of $L_D = 3.70$ m and a diffuser diameter of $D_D = 0.92$ m, respectively.

Contraction nozzle: The contraction section was designed with a square cross-section and outlet width equal to that of the test section, $W_{BC,OUT} = 0.56\,m$. An aspect ratio $AR_{BC} = 1$was adopted to prevent abrupt variations in cross-sectional area. A contraction ratio $RC = 7.7$was selected to avoid an excessively long wind tunnel, which would increase both manufacturing cost and installation space requirements. Equations 8 and 9 provided the inlet edge and the length of the contraction nozzle, calculated as $W_{BC,IN} = 1.56$ m and $L_{BC} = 1.56$ m respectively.

The contraction profile was defined by a third-order polynomial with an inflection point located at mid-length, as presented in Table 2.

Table 2 – Mathematical model of the contraction nozzle profile.

Match point ($X_m = 0.78$ m)	**Equation**
For $x < X_m$	$y = -0.4415x^3 + 0.7770$
For $x > X_m$	$y = -0.08830x^3 + 0.8232x^2 - 1.919x + 1.605$

The generated contraction nozzle profile is shown in Figure 1.

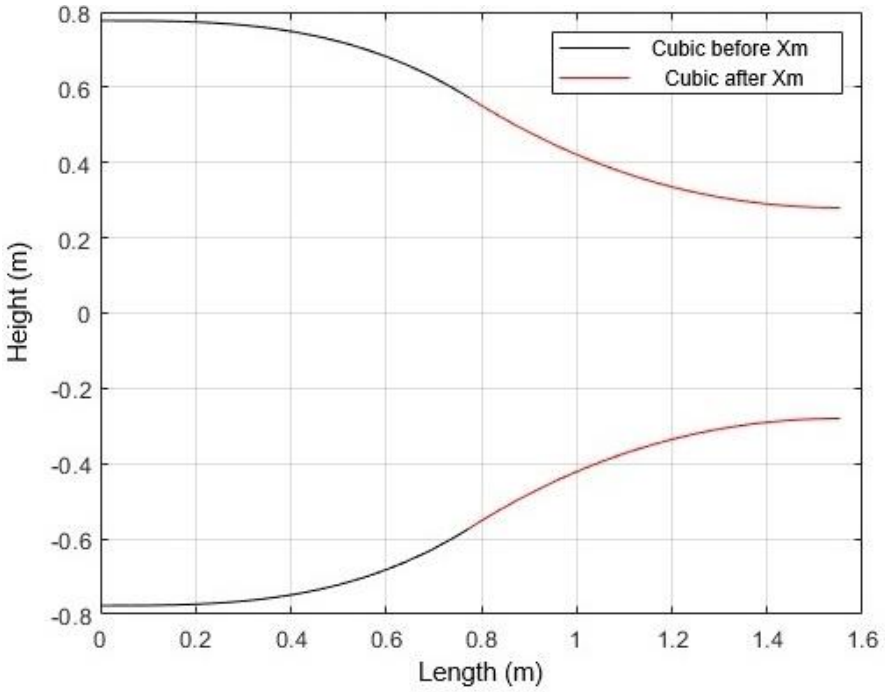

Figure 1 – Contraction nozzle profile defined by combined cubic polynomials.

Figure 2 presents a comparison between the generated combined-cubic curve and the mathematical profile proposed by Morel (1977).

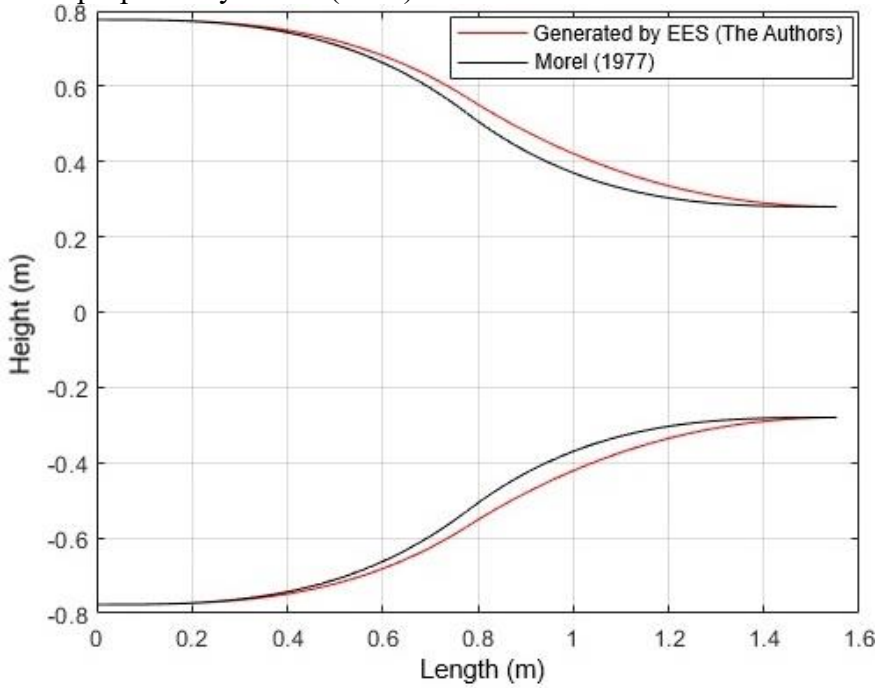

Figure 2 – Comparison between the generated curve and the curve proposed by Morel (1977).

The curve generated in EES, Figure 1, constrained by the conditions previously established in this study, closely matches the profile proposed by Morel (1977). Several studies reported in the literature adopt the profile proposed by Morel (1977) for the design of contraction nozzles, including the works of Assato *et al*. (2004), Martin (2019), and Zanoun (2017). Therefore, the contraction nozzle profile obtained in the present study exhibits promising characteristics, indicating strong agreement with profiles commonly reported in the literature.

4.2 Three-Dimensional Modeling

For the CFD analysis, the wind tunnel geometry was simplified by neglecting secondary details without compromising the representativeness of the model. This procedure was adopted to reduce the computational cost and to facilitate the mesh generation process. The three-dimensional geometry was developed using SolidWorks© and is presented in Figure 3.

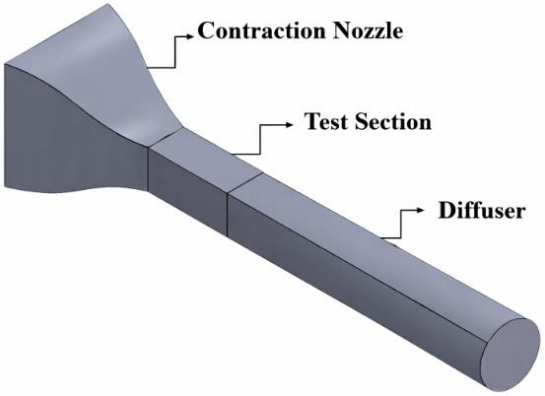

Figure 3 – 3D drawing of the simplified wind tunnel.

4.3 Pressure Loss Coefficients of the Wind Tunnel Components

Table 3 summarizes the pressure loss coefficients associated with each wind tunnel component.

Table 3 – Pressure loss coefficients.

Component	Loss Coefficient / (-)
Test Section	$K_{ST} = 0.019855$
Contraction Nozzle	$K_{BC} = 0.009594$
Diffuser	$K_{DF} = 0.02817$

The coefficients were calculated using the EES© software and subsequently employed to estimate the corresponding pressure losses, whose results are discussed in the following sections.

4.4 Computational Simulation

A baseline mesh was generated and employed in all simulations, with differences restricted to the near-wall treatment in order to properly resolve boundary-layer effects. For the Realizable k-ε turbulence model, two prism-layer regions were required to maintain y^+ within the recommended range.

The mesh generation process was conducted iteratively, with successive refinements performed until the predefined skewness criterion described in the Methodology was satisfied. Table 4 summarizes the main characteristics of the meshes adopted for each turbulence model.

Table 4 – Grid parameters.

Grid characteristics	SST k-ω	Realizable k-ε	Spalart-Allmaras
Number of elements	1877352	1192132	1877352
Number of nodes	1917256	1231496	1917256
First layer height / m	1.0×10^{-5}	Zone 1: 3.364×10^{-3} Zone 2: 9.953×10^{-4}	1.0×10^{-5}
Growth rate	1.3	Zone 1: 1.2 Zone 2: 1.2	1.3
Maximum number of layers	29	Zone 1: 6 Zone 2: 9	29

The meshes employed for the SST k-ω and Spalart-Allmaras models follow the same configuration and present characteristics comparable to those of the Realizable k-ε mesh, as illustrated in Figure 4.

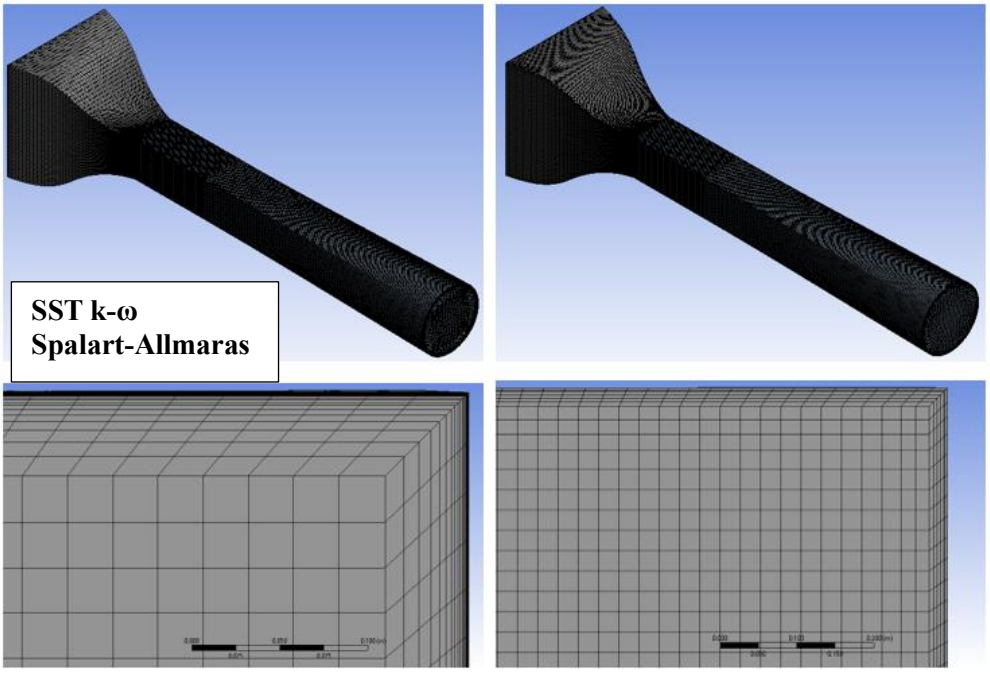

Figure 4 – Wind tunnel meshes and detail of the inflation at the contraction nozzle inlet.

In addition to monitoring the static and dynamic pressure at the contraction nozzle inlet and the velocity at the test section, the mass balance of the computational domain was also verified. The Flux Report available in the Solution module of ANSYS Fluent© indicated a maximum mass flow ratio on the order of 10^{-6}kg/s for all simulations, confirming global mass conservation within the domain and the reliability of the numerical convergence.

Table 5 presents the results obtained from the numerical simulations for the three turbulence models.

Table 5 – Results obtained from the numerical simulation.

Parameter	SST k-ω	Realizable k-ε	Spalart-Allmaras
Number of iterations	655	483	664
Simulated velocity / m/s (Test section)	63.24	63.22	63.24
Dynamic Pressure / Pa (Test section inlet)	2460.4	2458.5	2460.4
y^+range	< 0.90	31.3 - 256	< 0.91

The velocities obtained from the simulations with the three turbulence models exhibit close agreement with the design velocity of 63 m/s. The relative errors were 0.38% for the SST k-ω model, 0.35% for the Realizable k-ε model, and 0.38% for the Spalart-Allmaras model.

The dynamic pressure at the inlet of the test section presented a theoretical value of 2431.01 Pa. The relative errors obtained in the simulations were 1.21% for the SST k-ω model, 1.13% for the Realizable k-ε model, and 1.21% for the Spalart-Allmaras model.

Table 6 presents the pressure losses obtained for each wind tunnel component, considering the three turbulence models analyzed and the empirical value calculated.

Table 6 – Comparison between empirical and simulated pressure losses.

Component	SST k-ω / Pa	Realizable k-ε / Pa	Spalart-Allmaras / Pa	Empirical / Pa
Contraction Nozzle	58.54	54.12	55.50	0.3873
Test Section	42.26	44.55	44.40	48.28
Diffuser	173.42	145.85	155.75	68.47
Total	**274.22**	**244.52**	**255.66**	**117.14**

The total pressure losses predicted by the numerical simulations are higher than the empirical estimate. This discrepancy arises from the inherent simplifications of empirical correlations, which do not account for three-dimensional flow effects, separation phenomena, boundary-layer interactions, or additional losses associated with the boundary conditions imposed in the numerical model. Consequently, CFD simulations provide a more physically representative description of the flow and therefore predict higher dissipative effects than those obtained from empirical formulations.

Despite the differences relative to the empirical estimate, the three turbulence models yielded highly consistent predictions, indicating that the numerical evaluation of pressure losses is robust and largely independent of the turbulence model employed. Among the models investigated, the SST k–ω model produced the highest total pressure loss. This behavior is consistent with its improved capability to capture adverse pressure gradients and near-wall flow dynamics.

The diffuser was identified as the component that contributes most significantly to the overall pressure loss, due to the flow deceleration and the adverse pressure gradients inherently associated with this region (Mehta & Bradshaw, 1979). The largest discrepancy between empirical and numerical estimates occurs in the contraction nozzle, since the empirical formulation assumes an ideal contraction and considers only frictional losses.

Similar discrepancies between empirical predictions and numerical results have also been reported in previous studies. For instance, Aboelezz (2019) performed a comparative investigation involving empirical, computational, and experimental approaches for the evaluation of pressure losses in a low-speed wind tunnel. Table 7 summarizes the results reported by the author.

Table 7 – Comparison of pressure losses obtained using different methods.

Components	Empirical / Pa	SST k-ω / Pa	Experimental / Pa
Contraction Nozzle	5.1	75	72
Test Section	12.381	3	7
Diffuser	22.189	63	61
Total	**39.67**	**141**	**140**

Source: Adapted from Aboelezz (2019).

As shown in Table 7, the experimental results reported by the author exhibited close agreement with the numerical simulations, whereas the empirical correlations presented larger discrepancies, a behavior consistent with that observed in the present study. This trend arises because empirical methods rely on simplified representations of the flow and therefore tend to underestimate the associated losses, while numerical simulations are capable of capturing three-dimensional effects and complex flow interactions more accurately. Consequently, the present results reinforce the reliability of the numerical simulations and the overall consistency of the analysis.

Figure 5 presents the variation of velocity magnitude and dynamic pressure, whereas Figure 6 illustrates the distribution of static pressure along the wind tunnel, obtained using the SST k–ω turbulence model.

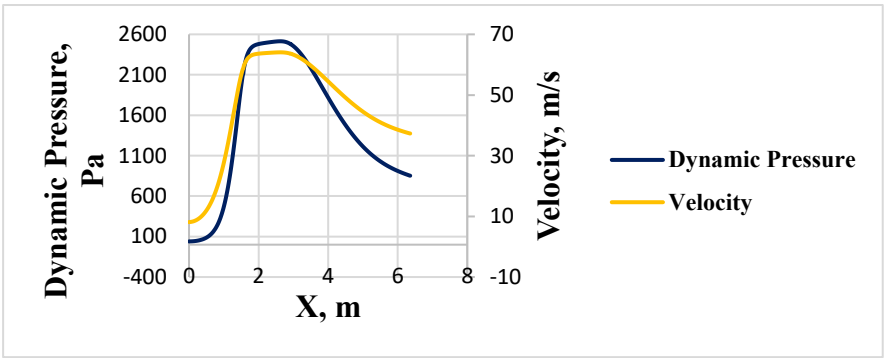

Figure 5 – Variation of velocity and dynamic pressure along the wind tunnel.

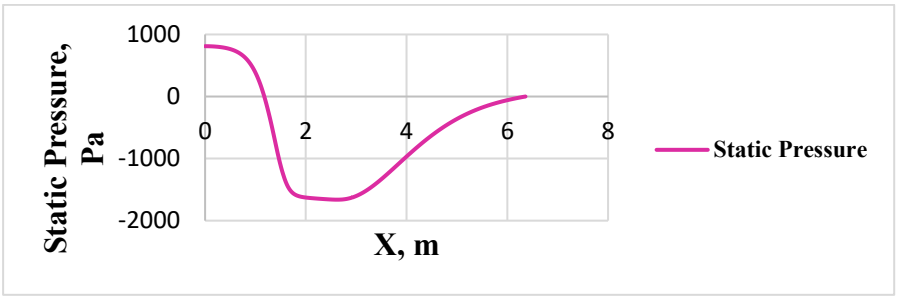

Figure 6 – Variation of static pressure along the wind tunnel.

Figures 5 and 6 show a pronounced increase in velocity within the contraction section, accompanied by a corresponding rise in dynamic pressure and a decrease in static pressure, consistent with the Bernoulli's principle. In the test section, these variables remain nearly constant, indicating a stabilized and uniform flow field. Downstream of this region, a gradual reduction in velocity and dynamic pressure is observed, along with a recovery of static pressure, which is characteristic of the flow expansion occurring in the diffuser. It should be noted that the remaining turbulence models exhibited similar trends; therefore, only one representative case is presented.

Figures 7, 8, and 9 illustrate the velocity and static pressure fields in the symmetry plane of the wind tunnel for the SST k-ω turbulence model, Realizable k-ε turbulence model, and Spalart-Allmaras turbulence model, respectively.

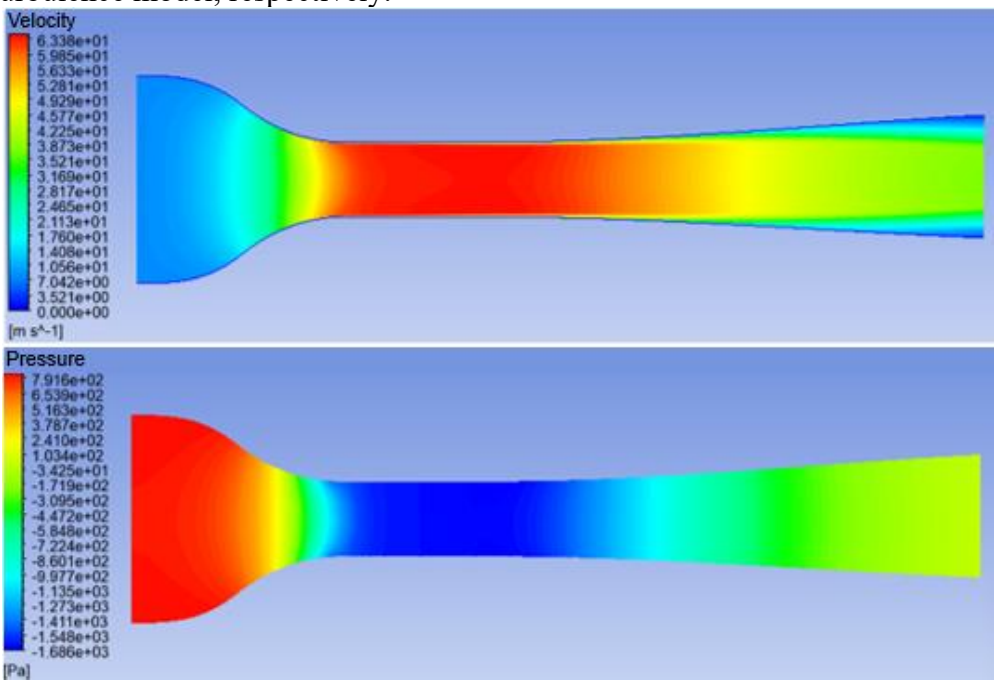

Figure 7 – Profiles obtained using the SST k-ω model.

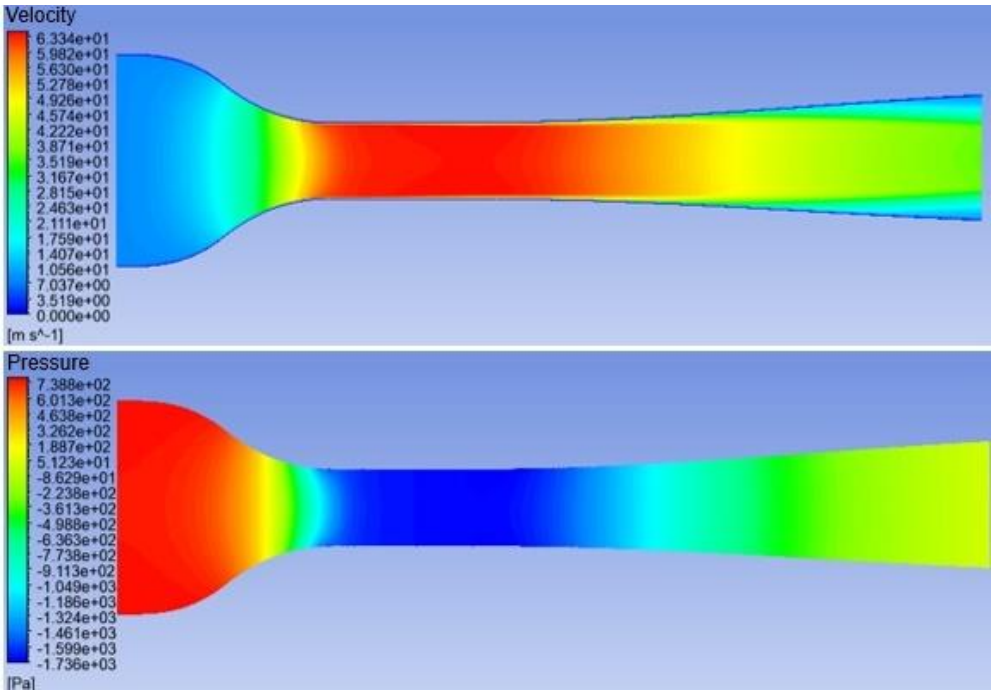

Figure 8 – Profiles obtained using the Realizable k-ε model.

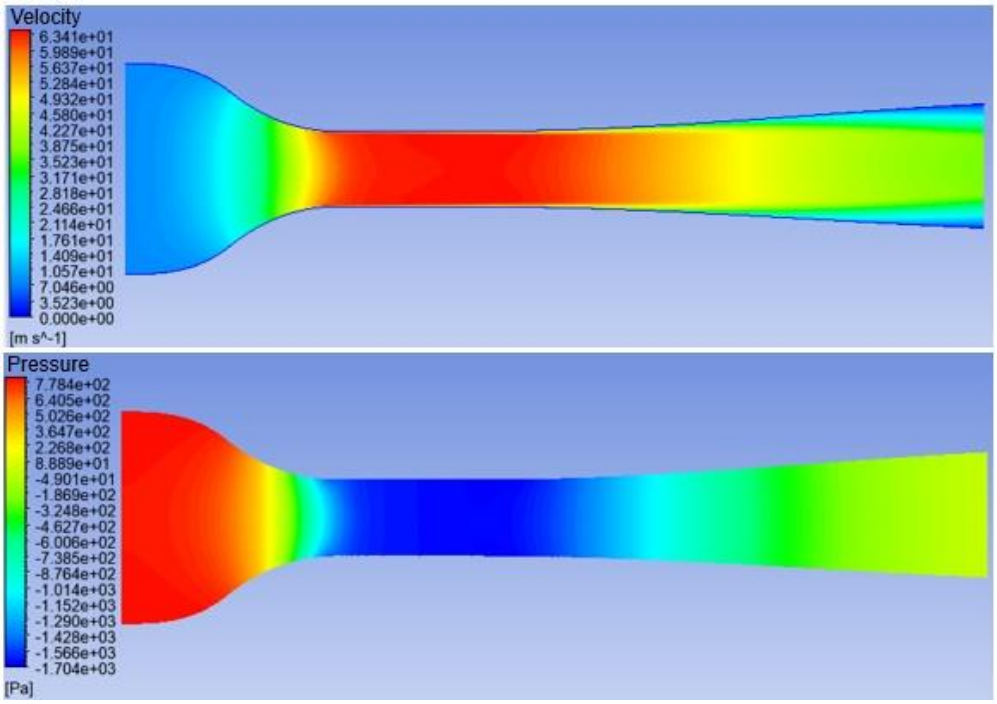

Figure 9 – Profiles obtained using the Spalart-Allmaras model.

All fields exhibit similar behavior: the velocity increases in the contraction nozzle region, while the static pressure decreases, reflecting consistency with Bernoulli's principle. In the test section, the flow remains nearly uniform in all cases, indicating stable conditions suitable for experimental analysis. In the diffuser, the velocity gradually decreases while the static pressure increases, demonstrating the recovery of the flow pressure. The small variations observed among the distributions predicted by the turbulence models reflect differences in turbulence modeling; however, these differences do not alter the overall flow trend along the wind tunnel.

Figures 10, 11, and 12 present the streamlines along the wind tunnel for the three turbulence models.

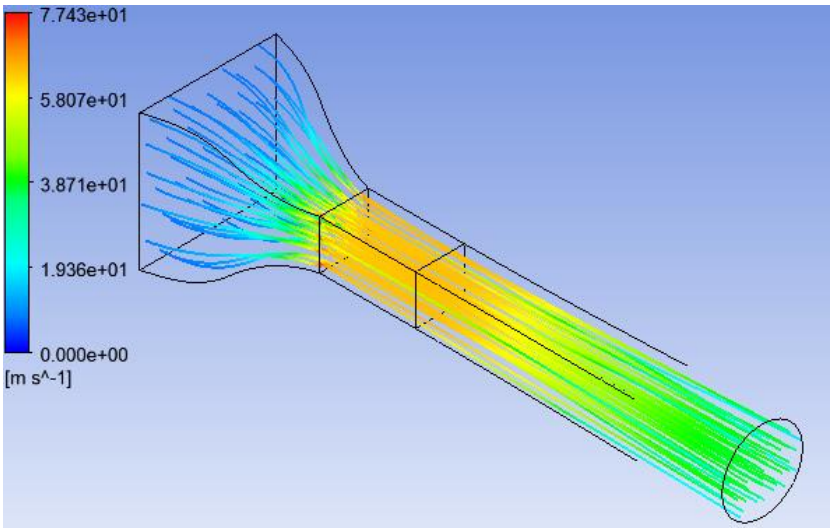

Figure 10 – Streamlines obtained using the SST k-ω model.

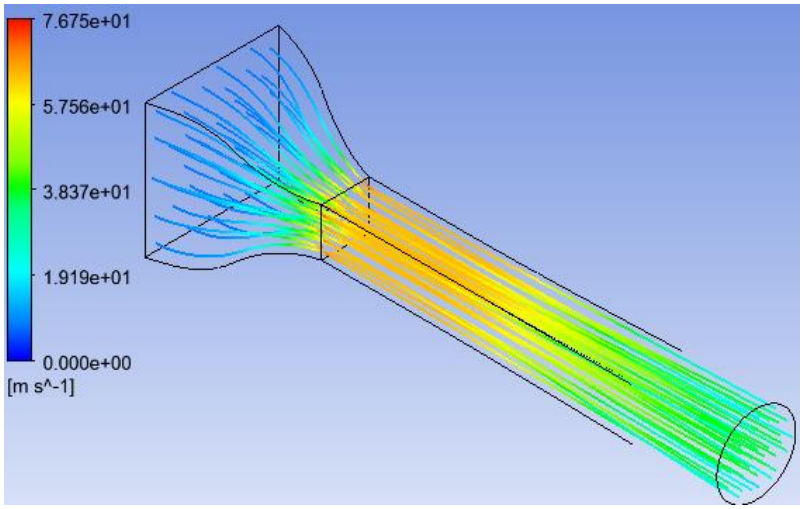

Figure 11 – Streamlines obtained using the Realizable k-ε model.

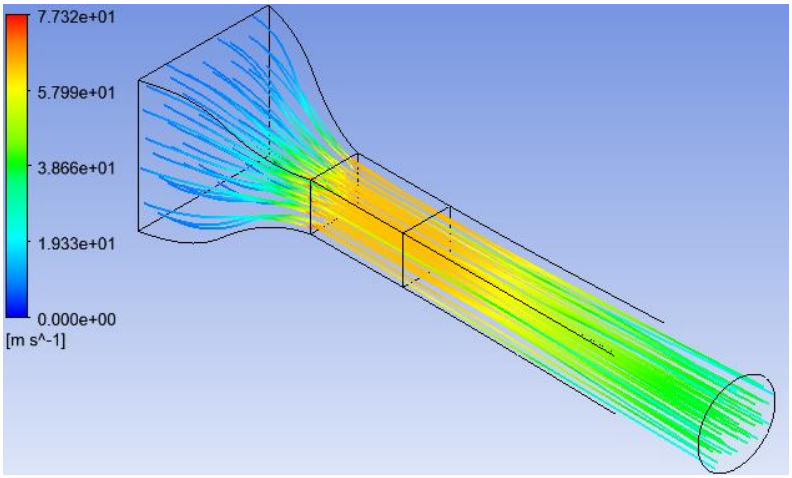

Figure 12 – Streamlines obtained using the Spalart-Allmaras model.

Figures 10, 11, and 12 show that the flow remains fully attached throughout the wind tunnel, with no evidence of recirculation or flow separation. This behavior indicates that the geometric configuration of the contraction, test section, and diffuser ensures stable flow development along the entire domain.

Figures 13, 14, and 15 present the velocity profiles extracted along a vertical line located at the center of the contraction nozzle, test section, and diffuser, respectively, for the three turbulence models analyzed.

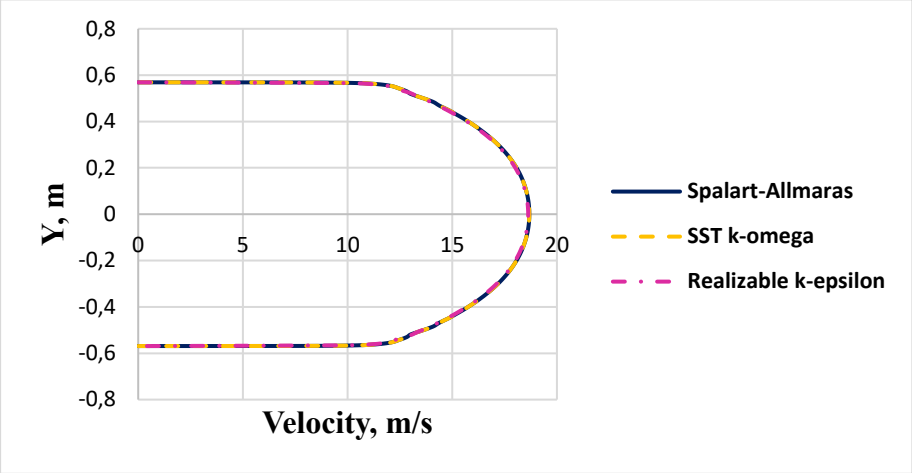

Figure 13 – Velocity profiles in the contraction nozzle.

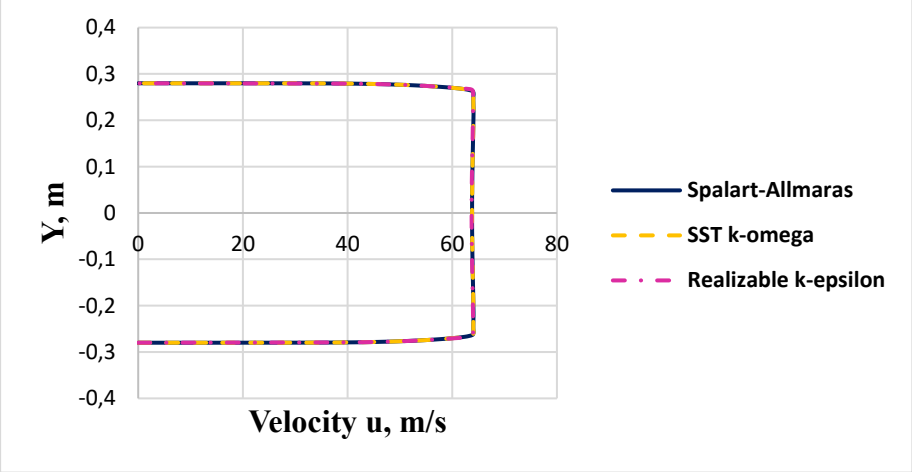

Figure 14 – Velocity profiles in the test section.

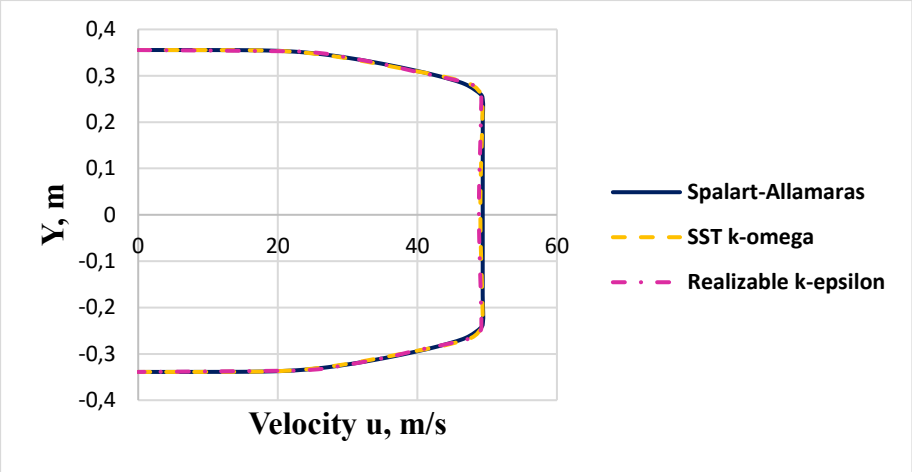

Figure 15 – Velocity profiles in the diffuser.

Figures 13, 14, and 15 show that the three turbulence models produced nearly identical velocity profiles in all analyzed regions, indicating that the flow field was consistently predicted regardless of the turbulence model employed.

In the test section, the velocity profiles remain essentially uniform, with values close to the design velocity of 63 m/s, confirming the development of a well-established and homogeneous flow. Within the boundary layer region, the velocity decreases toward zero due to the no-slip condition at the wall.

The largest differences among the turbulence models occur in the diffuser region, which is consistent with the expected physical behavior, as this region is characterized by adverse pressure gradients associated with flow deceleration. Under such conditions, the SST k-ω model generally provides improved predictions, as it is better suited to capture flows subjected to boundary-layer separation. Nevertheless, the discrepancies among the models remain minimal, indicating that, for the simulated conditions, all turbulence models were able to adequately reproduce the overall flow behavior within the wind tunnel.

5. Conclusion

This study presents the design of the main components of a suction-type wind tunnel and a numerical investigation of the flow behavior using ANSYS Fluent© with three turbulence models: SST k-ω, Realizable k-ε, and Spalart-Allmaras. Based on the theoretical backgrounded presented, the parameters and dimensions of the contraction nozzle, test section, and diffuser were determined, together with their respective pressure losses. The numerical analysis aimed to compare the results obtained for velocity, pressure, and pressure losses with theoretical predictions, in order to evaluate the influence of the turbulence model selection on simulation accuracy.

The numerical results exhibited strong agreement among the turbulence models considered. The discrepancy between the calculated value and the numerical prediction for the mean velocity at the test section inlet remained below 0.4%, corresponding to 0.38% for the SST k–ω and Spalart-Allmaras models and 0.35% for the Realizable k–ε model. The relative error associated with the dynamic pressure at the test section inlet, compared with the value obtained from the Bernoulli equations, remained below 1.25%, reaching 1.21% for the SST k–ω and Spalart-Allmaras models and 1.13% for the Realizable k–ε model. In addition, the velocity and static pressure contours, as well as the velocity profiles along the wind tunnel sections, displayed highly consistent distributions. Under the investigated conditions, the flow behavior exhibited limited sensitivity to the turbulence model employed. Although the Spalart-Allmaras model was originally developed for external aerodynamic applications, it produced predictions comparable in accuracy to those obtained with the two-equation models, even at the relatively high operating velocity of 63 m/s in the test section. This performance can be attributed to the stable flow regime observed throughout the tunnel, with no evidence of boundary-layer separation, which allowed the model to accurately reproduce the velocity and pressure fields.

The pressure losses obtained through CFD exceeded the empirical estimates. This behavior is consistent with reports in the literature and arises from the simplifying assumptions inherent to analytical correlations, which neglect three-dimensional effects, local velocity variations, and boundary-layer-related phenomena. Consequently, the numerical simulations provide a more realistic representation of the flow behavior inside the wind tunnel and yield physically more consistent predictions.

Among the evaluated models, the Spalart-Allmaras formulation represents a suitable alternative for this application, combining satisfactory predictive capability with reduced computational cost. Nevertheless, this performance may not extend to more complex flow configurations, for which two-equation turbulence models generally offer greater robustness. Therefore, the turbulence model selection should always consider the specific characteristics of the flow under investigation.

Acknowledgements

The authors thank of Federal University of Viçosa (UFV). This paper was carried out with the support of the Minas Gerais State Research Support Foundation (FAPEMIG) and Arthur Bernardes

Foundation (FUNARBE) - Process PPE-00023-21, Government of Minas Gerais - Seinfra-MG, Railway Technological Development Nucleo of the State of Minas Gerais -NDF and CNPq.

References

Aboelezz, A. (2019). Low Speed Wind Tunnel Design and Optimization Using Computational Techniques and Experimental Validation. *INCAS BULLETIN*, 3–13. https://doi.org/10.13111/2066-8201.2019.11.2.1

Almeida, O. D., Miranda, F. C. D., Ferreira Neto, O., & Saad, F. G. (2018). Low subsonic wind tunnel-Design and construction. *Journal of Aerospace Technology and Management*, *10*, e1018. https://doi.org/10.5028/jatm.v10.716

Ansys Inc. (2013). *Ansys Fluent User's Guide, Release 15.0.*

Ansys Inc. (2021). *Ansys Fluent Theory Guide, Release 2021 R2*. https://dl.cfdexperts.net/cfd_resources/Ansys_Documentation/Fluent/Ansys_Fluent_Theory_Guide.pdf

Arifuzzaman, M., & Mashud, M. (2012). Design construction and performance test of a low cost subsonic wind tunnel. *IOSR Journal of Engineering*, *2*(10), 83-92. https://www.researchgate.net/publication/271251293_Design_Construction_and_Performance_Test_of_a_Low_Cost_Subsonic_Wind_Tunnel

Assato, M., Girardi, R., Fico, N., Mello, O., & Komatsu, P. (2004). Research Wind Tunnel of the Aeronautical Institute of Technology: Conceptual Design and Calibration. In *42nd AIAA Aerospace Sciences Meeting and Exhibit*, Reno, USA. https://doi.org/10.2514/6.2004-724

Barbosa, H. V. de S., Campos, J. C. C., Siqueira, A. M. de O., Hilário, C. V., Faria, N. de O., Dias, B. de A., & Moreira, P. H. B. C. (2021). Computational numerical analysis of drag force on a standard AeroDesign wing in accordance with winglet application. *The Journal of Engineering and Exact Sciences*, *7*(4). https://doi.org/10.18540/jcecvl7iss4pp13231-01-13e

Barlow, J. B., Rae, W. H., & Pope, A. (1999). *Low-speed wind tunnel testing*. John Wiley & Sons.

Bell, J. H., & Mehta, R. D. (1988). *Contraction design for small low-speed wind tunnels* (No. NASA-CR-177488).

Bell, J. H., & Mehta, R. D. (1989). Boundary-layer predictions for small low-speed contractions. *AIAA Journal*, *27*(3), 372-374. https://doi.org/10.2514/3.10122

Cengel, Y. A., & Cimbala, J. M. (2007). *Mecânica dos Fluidos: Fundamentos e Aplicações*. AMGH Editora.

Dantas, A. F. D. M. (2017). *Análise comparativa entre modelos de turbulência utilizando Ansys-Fluent para obtenção dos coeficientes aerodinâmicos do perfil Eppler 423*. Monografia, Universidade Federal Rural do Semi-Árido, Mossoró, RN, Brail.

Oliveira, R. P. de, Dalmolin, V., & Haus, T. L. (2015). FABRICAÇÃO DE UM TÚNEL DE VENTO DE CIRCUITO ABERTO PARA TESTES VISUAIS EM MODELOS GEOMÉTRICOS. *Memorial TCC Caderno da Graduação*, *1*(1), 443-459. https://memorialtcccadernograduacao.fae.edu/cadernotcc/article/view/28

Derbunovich, G. I., Zemskaya, A. S., Repik, E. U., & Sosedko, Y. P. (1987). Effect of flow contraction on the level of turbulence. *Fluid Dynamics*, *22*(2), 289–294. https://doi.org/10.1007/bf01052265

Fiuza, G. C. C., & Rezende, A. L. T. (2019). Comparação entre modelos de turbulência K-ω aplicados em um escoamento em canal com junção T. *Revista Militar de Ciência e Tecnologia*, *34*(9). http://www.ebrevistas.eb.mil.br/CT/article/view/3382/2752

Fox, R. W., Pritchard, P. J., & McDonald, A. T. (2010). *Introdução à Mecânica Dos Fluidos*. Grupo Gen-LTC.

Girardi, R. M., Fico Jr, N. G. C. R., Mello, O. A. F., & Komatsu, P. (2002, August). Design of the Research Subsonic Wind Tunnel of the aeronautical Institute of Technology. In *Proceedings of the Mechanical Engineering National Congress (CONEM 2002)*, João Pessoa, PB, Brasil.

Hussain, A. K. M. F., & Ramjee, V. (1976). Effects of the axisymmetric contraction shape on incompressible turbulent flow. *Journal of Fluids Engineering*, *98*(1), 58-68. https://doi.org/10.1115/1.3448210

Kareem, A. A., Abbas, M. K., & Khammas, F. A. (2021). Aerodynamic Study of Low-Speed Wind Tunnel Contraction Section: Design and Manufacturing. *IOP Conference Series: Materials Science and Engineering*, *1094*(1), 012077. https://doi.org/10.1088/1757-899x/1094/1/012077

Lins, D. R. (2018). *Dimensionamento de um túnel de vento subsônico*. Monografia, Universidade Federal do Ceará, Fortaleza, CE, Brasil.

Mathew, J., Bahr, C., Carroll, B., Sheplak, M., & Cattafesta, L. (2005). Design, fabrication, and characterization of an anechoic wind tunnel facility. In *Proceedings of the 11th AIAA/CEAS Aeroacoustics Conference (26th AIAA Aeroacoustics Conference)* (AIAA Paper No. 2005-3052). https://doi.org/10.2514/6.2005-3052

Martin, J. S. (2019). *Nozzle design for a small, low-speed, closed-return wind tunnel* (Monografia de Bacharelado, Houghton College, Department of Physics). Houghton College.

Matos, C. C., & Botelho, R. D. (2008). A influência da aerodinâmica no design. *Actas de Diseño*, (4).

Mehta, R. D., & Bradshaw, P. (1979). Design rules for small low speed wind tunnels. *The Aeronautical Journal*, *83*(827), 443-453. https://doi.org/10.1017/S0001924000031985

Menter, F. R. (1994). Two-equation eddy-viscosity turbulence models for engineering applications. *AIAA journal*, 32(8), 1598-1605. https://doi.org/10.2514/3.12149

Menter, F. R. (2011). Turbulence modeling for engineering flows. *Ansys, Inc*. https://www.ozeninc.com/wp-content/uploads/2021/01/Turbulence-Modeling-for-Engineering-Flows.pdf

Moreira, G. A. A., Viana, A. L., & Vale, R. M. (2014). ANÁLISE DA TURBULÊNCIA EM MODELO NUMÉRICO PARA DETERMINAÇÃO DO POTÊNCIAL EÓLICO. In *V Anais Congresso Brasileiro de Energia Solar-CBENS*, Recife, Brasil.

Morel, T. (1977). Design of Two-Dimensional Wind Tunnel Contractions. *Journal of Fluids Engineering*, *99*(2), 371-377. https://doi.org/10.1115/1.3448764

Núñez, G. J. Z., Souza, A. M. L., & Rocha, M. M. (2012). Uso do túnel de vento como ferramenta de projeto no design aerodinâmico. *Design & Tecnologia*, *2*(4), 10-23. https://doi.org/10.23972/det2012iss04pp10-23

Pereira, J. D. (2011). *Wind Tunnels: Aerodynamics, Models, And Experiment*. Nova Science Publishers.

Reddy, H., & Subramanian, B. (2025). Aerodynamic design of three-dimensional contraction for low-speed wind tunnel. *Proceedings of the Institution of Mechanical Engineers, Part G: Journal of Aerospace Engineering*, *0*(0), 1-17. https://doi.org/10.1177/09544100251329079

Rezende, A. L. T. (2009). *Análise numérica da bolha de separação do escoamento turbulento sobre placa plana fina inclinada*. Tese de Doutorado, Pontifícia Universidade Católica, Rio de Janeiro, RJ, Brasil.

Santos, A. A. C. (2012). *Simulação numérica de perfis alares utilizados em aerogeradores de eixo vertical*. Dissertação de Mestrado, Faculdade de Ciências e Tecnologia - Universidade de Coimbra, Coimbra, Portugal.

Schinestzki, W. N., da Luz, L. B., Zart, J. C. I. G., & da Silva, A. L. (2018). Projeto Conceitual de Túnel de Vento Aerodinâmico de Sucção. *1º Congresso Espacial Brasileiro – Edição Especial Plêiade*, Foz do Iguaçu, Paraná, Brasil. https://www.researchgate.net/publication/330657998_Projeto_Conceitual_de_Tunel_de_Vento_Aerodinamico_de_Succao

Shelil, N. (2021). 2D Numerical Simulation Study of Airfoil Performance. *Wind Energy Science Discussions*, *2021*, 1-19. https://doi.org/10.5194/wes-2021-45

Shih, T. H., Liou, W. W., Shabbir, A., Yang, Z., & Zhu, J. (1994). A new k-ϵ eddy viscosity model for high Reynolds number turbulent flows. *Computers & fluids*, *24*(3), 227-238. https://doi.org/10.1016/0045-7930(94)00032-T

Soares, R. F. (2013). *Estudo Fluidodinâmico Computacional (CFD) Aplicado à Aerodinâmica do Esporte Automobilístico*. Monografia, Universidade Tecnológica Federal do Paraná, Cornélio Procópio, PR, Brasil.

Souza, C. A. de, Campos, J. C. C., Siqueira, A. M. de O., Treto, P. C., Tibiriça, A. M. B., Rosa, H. M. P., & Brito, R. F. (2023). Experimental Simulation of a Tennis Ball using Wind Tunnel. *The Journal of Engineering and Exact Sciences*, *9*(1), 15179-01e. https://doi.org/10.18540/jcecvl9iss1pp15179-01e

Spalart, P., & Allmaras, S. (1992). A one-equation turbulence model for aerodynamic flows. In *30th Aerospace Sciences Meeting and Exhibit*, Reno, USA. https://turbmodels.larc.nasa.gov/Papers/RechAerosp_1994_SpalartAllmaras.pdf

Su, Y. X. (1991). Flow analysis and design of three-dimensional wind tunnel contractions. *AIAA journal*, *29*(11), 1912-1920. https://doi.org/10.2514/3.10818

Treto, P. C., Campos, J. C. C., Ramírez, K. S., Minette, L. J., & Siqueira, A. M. de O. (2020). Utilización del modelo DES, con base en el modelo de turbulencia Spalart-Allmaras en el análisis del perfil S809. *The Journal of Engineering and Exact Sciences, 6*(3), 207–213. https://doi.org/10.18540/jcecvl6iss3pp0207-0213

Van Dommelen, R. (2013). *Design of an atmospheric boundary layer wind tunnel*. Dissertação de Mestrado, Universidade Tecnológica de Eindhoven, Eindhoven, Holanda. http://rinkavandommelen.nl/WindtunnelThesisRinka.pdf

Versteeg, H. K., & Malalasekera, W. (2007). *An introduction to Computational Fluid Dynamics: The Finite Volume Method*. Pearson Education.

Wattendorf, F. L. (1938). *Factors influencing the energy ratio of return flow wind tunnels*. In Proceedings of the 5th International Congress for Applied Mechanics. Cambridge.

Wilcox, D. C. (1998). *Turbulence modeling for CFD*. DCW Industries.

Zanoun, E. S. (2018). Flow characteristics in low-speed wind tunnel contractions: Simulation and testing. *Alexandria Engineering Journal, 57*(4), 2265–2277. https://doi.org/10.1016/j.aej.2017.08.024

Zart, J. C. I. G., da Luz, L. B., Schinestzki, W. N. (2018). *Projeto de túnel de vento aerodinâmico de sucção*. Monografia, Universidade Federal de Santa Maria, Santa Maria, RS, Brasil.